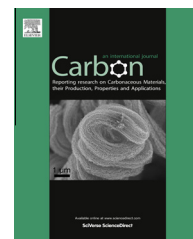


Available at www.sciencedirect.com

ScienceDirect

journal homepage: www.elsevier.com/locate/carbon

Multi-layer graphene obtained by high temperature carbon implantation into nickel films

G. Gutierrez^a, F. Le Normand^{a,*}, D. Muller^a, F. Aweke^a, C. Speisser^a, F. Antoni^a
Y. Le Gall^a, C.S. Lee^b, C.S. Cojocar^c

^a ICube-Laboratoire des sciences de l'Ingénieur, de l'Informatique et de l'Imagerie, Université de Strasbourg-CNRS, 23, rue du Loess, 67037 Strasbourg Cedex, France

^b Graphene Center, Samsung Advanced Institute of Technology, Yongin 446-712, South Korea

^c LPICM-Laboratoire de Physique des Interfaces et des Couches Minces, Ecole Polytechnique-CNRS, 91128 Palaiseau Cedex, France

ARTICLE INFO

Article history:

Received 24 February 2013

Accepted 31 July 2013

Available online 21 August 2013

ABSTRACT

We present a study of carbon implantation in a stacked layered substrate made of Ni(200 nm)/SiO₂(300 nm)/Si(100). The carbon atoms have energy of 20 keV. Simultaneous or subsequent heat treatment is performed in the 450–600 °C range. The carbon dose was set to be 4 equivalent graphene monolayers (EGM). Most of the carbon implanted diffuses directly to the surface, forming multi-layer graphene (MLG). A progressive structuration of these graphitic fragments occurs with the increase of the implantation temperature. However, this structuration is more pronounced if the thermal treatment is performed in situ following the carbon implantation at room temperature. The mean MLG thickness, corresponding to around 4–5 EGM, was measured by angular X-ray Photoemission Spectroscopy. Moreover, the overall carbon concentration inside and at the limits of the nickel films, determined by nuclear reaction analysis (NRA), is in the 7–10 EGM range. This concentration depends on the temperature but it exceeds surprisingly the expected carbon concentration. This discrepancy shows that some carbon is incorporated along the different steps. NRA analyses of the preparation confirm this point. To obtain large film, the presented results stress the interest to better understand the full system carbon–nickel in the preparation of MLG at each step of the process.

© 2013 Elsevier Ltd. All rights reserved.

1. Introduction

The graphene is a 2D hexagonal network of sp²-hybridized carbon atoms whose successful preparation has been reported recently [1]. In a very short time, many outstanding electronic transport properties have been reported on the graphene prepared by exfoliation from Highly Oriented Pyrolytic Graphite (HOPG) [2–4]. To achieve these properties is however strongly dependent on the preparation and the handling of this material [5]. Moreover the exfoliation method is not scalable and not reproducible. Therefore many alternative

elaboration processes have been described in the literature, based on chemical synthesis [6], on the high temperature Si layer evaporation from a SiC monocrystalline surface [7–9], on the lower temperature surface segregation of carbon absorbed into metals, like Ni or Ru, by Chemical Vapor Deposition (CVD) [10–17], on the carbon adsorption on copper by CVD [18–19], or on the bulk diffusion of carbon across metallic matrices from solid sources [20–23]. All these methods have currently their advantages and their drawbacks, which are depending on the expected application. In this work, we will systematically study a process derived from the CVD carbon

* Corresponding author. Fax: +33 3 88 10 6546.

E-mail address: francois.le-normand@unistra.fr (F. Le Normand).
0008-6223/\$ - see front matter © 2013 Elsevier Ltd. All rights reserved.
<http://dx.doi.org/10.1016/j.carbon.2013.07.106>

surface segregation on a metallic matrix. In this method of elaboration, recently patented [24] and published [25–28], the carbon was introduced into a carbon-diffusive metallic matrix like Ni by ion implantation. After the implantation step, thermal treatments were achieved to diffuse carbon towards either the surface or even to the interface between the film and the substrate. This new way of preparation of graphene or multi-layer graphene (MLG) displays potentially many advantages over the CVD process: (i) Accurate and uniform control of the carbon dose; (ii) Accurate depth localization of the carbon inside the metallic matrix through managing the ion energy, therefore the growth of graphene could occur at the interface metal/substrate rather than at the surface according to the energy of carbon ion, to the carbon solubility and to the carbon diffusion into the matrix; (iii) No necessity for gaseous decomposition of the carbon-precursor molecule like in CVD; (iv) Direct integration into electronic devices of the interface graphene after dissolution of the metallic film is possible. Thus this process may be fully compatible with current microelectronic processes and the silicon technology. Literature investigations have shown that the formation of multi-layer graphene (MLG) was indeed obtained [25–28]. However the implantations were performed at room temperature followed by a thermal post-treatment. We present here for the first time high temperature (450–600 °C) implantation of carbon, thus mixing into one single step carbon implantation and thermal post treatment. By this high temperature process, it is therefore expected to activate the carbon diffusion and to minimize the implantation defects. Another report has been devoted to the influence of carbon dose and thermal post-treatments within 450–900 °C [29] after implantation at room temperature.

2. Experimental

Si(100) substrates were oxidized at 1100 °C in order to grow a 300 nm thermal-SiO₂ layer. To remove the organic residues off the substrates, the substrates were dipped into trichloroethylene while heating at 100 °C during 30 min, rinsed successively into acetone, isopropyl alcohol, cleaned in a Piranha solution 30 min at 150 °C, rinsed with deionized water and finally dried under nitrogen. After this cleaning step, 200 nm thick Ni films were evaporated by electron beam deposition at room temperature with a deposition rate lower than 0.3 nm s⁻¹ at a base pressure of 2.7×10^{-7} mbar. ¹²C ions at an energy of 20 keV and a fluence of 1.4×10^{16} at.cm⁻² corresponding to around 4 equivalent graphene monolayers (EGM; one EGM corresponds to 3.6×10^{15} at.cm⁻²) were implanted on these Ni (200 nm)/SiO₂ (300 nm)/Si samples. These implantations were achieved on the 200 kV EATON implanter of ICube provided with a heated substrate holder in Inconel alloy. The temperature of the surface sample was calibrated with one thermocouple permanently settled on the back near the surface of the substrate holder and a filament extinction pyrometer monitoring directly the sample surface temperature.

In order to decorrelate the synergetic effect of implantation and temperature, two kinds of sample were prepared. The first set of samples was implanted at a pressure vacuum of 2×10^{-6} mbar at 450 °C, 525 °C and 600 °C, respectively.

They were further named I-T where T is the implantation temperature. The samples were maintained at each temperature for 1 h which corresponds to the implantation duration. Other samples named I-RT and I-RT-600 were implanted at room temperature and subsequently annealed at 600 °C inside the implantation chamber in similar conditions (4 EGM, 2×10^{-6} mbar, 1 h), respectively. In both cases, the heating and cooling rates were estimated to be around 60 °C min⁻¹. The implantation conditions were determined using the SRIM 2010 software which simulates the carbon profile at room temperature for an amorphous material [30]. The carbon distribution profile results in a quasi-Gaussian curve centered around 27 nm depth. The sputtering due to implantation has been determined to 2.9 nm by using SRIM. This result is in good agreement with the Rutherford Backscattering spectra (RBS) obtained before and after implantation which highlight no significant thickness evolution of the Ni film (Supplementary Materials S1).

A scheme of the overall process is given in Fig. 1.

Ion beam analyses were performed using the 4MV Van De Graff accelerator facility of ICube. RBS was used to determine the thicknesses of the Ni and SiO₂ layers before and after the implantation and/or thermal post-treatments. RBS experiments were carried out with a 2 MeV incident alpha particles beam (1×1 mm²) and a 160° scattering angle. Moreover, to determine the evolution of C and O concentrations after each treatment, Nuclear Reaction Analyses (NRA) were performed. The ¹²C(d, p)¹³C, ¹⁶O(d, p)¹⁷O and ¹⁶O(d, p)¹⁷O reactions were investigated with a 900 keV deuterons beam (1×1 mm²). A 150 mm² silicon surface barrier detectors was mounted at an angle of 150° to the beam direction resulting in a total solid angle of $\Omega \sim 60$ msr. An absorber of 11.8 μm Mylar foil was attached above the detector to stop the alpha particles generated by the ¹⁶O(d, α)¹⁴N reaction and the backscattered deuterons particles. The experimental spectra were calibrated by using bare SiO₂ and SiC samples for oxygen and carbon nuclear reactions, respectively, and the spectra were then simulated with the SAM software [31]. The error bar was estimated to around 2 EGM. Due to the low depth resolution of this analysis technique, we are not able to differentiate between the carbon surface and the carbon diluted into the Ni layer.

To characterize the surface of the implanted samples, SEM observations were carried out using a Scanning Electron Microscope (Philips XL-30S) in the Secondary Electron Image mode at low voltages (1 and 3 kV) more sensitive to the chemical contrast.

The Atomic Force Microscopy (AFM) measurements were performed on a NT-MDT Stand Alone “SMENA” set-up used in the resonant mode AFM Semicontact. Non-Contact “Golden” Silicon Cantilever NSG11 scanning probes were used with a minimum scanning step of 0.012 nm.

Raman spectroscopy was carried out using a Horiba spectrometer LabRam at 532 nm equipped with a CCD camera. Spectra were recorded using a 100× magnification, with a power energy of 0.93 mW and a fluence of 2.25 mW μm⁻². Above this fluence, damages of the graphene film might be observed [32].

X-ray photoemission spectra were recorded with a 150 mm hemispherical detector VSW with an overall resolution of 0.65 eV under a base pressure of 5×10^{-9} mbar using a

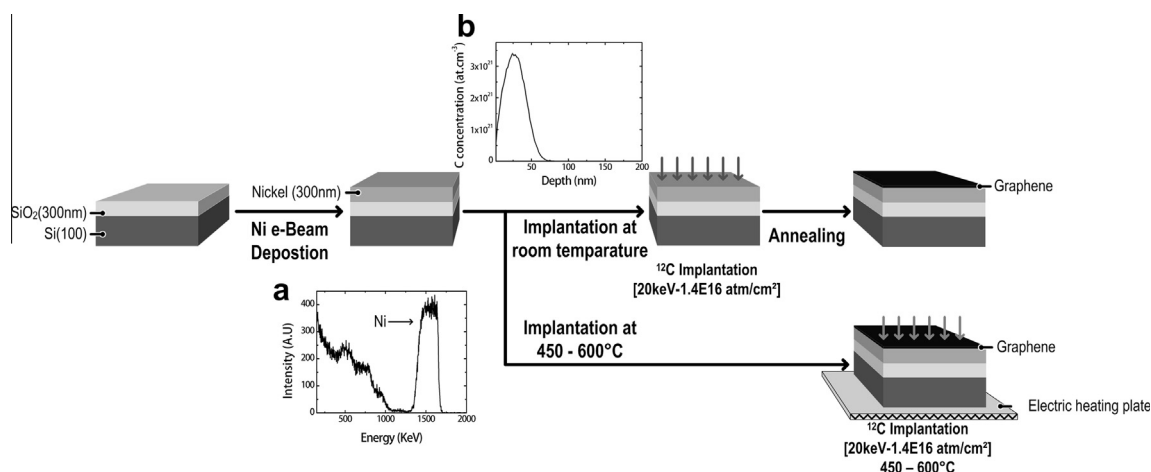


Fig. 1 – Scheme of the full process of MLG preparation by carbon implantation. In insert (a) RBS profile after carbon implantation at room temperature and (b) SRIM simulation of the carbon distribution profile is displayed after implantation at 20 keV into Ni(200 nm)/SiO₂(300 nm)/Si.

monochromatic AlK α source. Energy references are set using the HOPG C1s core level at 284.6 eV.

3. Results

NRA experiments are carried out at each step of the preparation process to determine the level of carbon impurity in addition to the implanted carbon. Fig. 2 displays the NRA spectra obtained on samples at different step of the process: SiO₂(300 nm)/Si, Ni(200 nm)/SiO₂(300 nm)/Si before carbon implantation and I-RT samples. To simplify the figure, only a set of characteristic experimental NRA contributions is displayed in Fig. 2. The signals at 1183, 2073 and 2728 keV are due to the ¹⁶O(d, p)¹⁷O, ¹⁶O(d, p)¹⁷O and ¹²C(d, p)¹³C nuclear reactions, respectively.

We can observe an increasing carbon signal after each treatment and no significant oxygen signal evolution of the silicon dioxide. The shift of the oxygen signals to a lower energy on Ni(200 nm)/SiO₂(300 nm)/Si samples is due to the covering of the SiO₂ layer by the nickel film. The carbon concentrations obtained by fitting these experimental spectra with the SAM software are reported in Table 1, including in addition the I-450, I-525, I-600 and I-RT-600 samples. The carbon concentrations are converted to EGM using the calibration signal of SiC with the known value for 1 EGM quoted to

$3.6 \times 10^{15} \text{ at.cm}^{-2}$ (Table 1). We also specified the net increase of carbon (EGM) at each step i, $\Delta(C_i - C_{i-1})$.

Within the experimental conditions used throughout this work, the incorporation of some carbon as impurity cannot be avoided. This carbon adds to the 4 EGM of carbon implanted. Even the bare SiO₂(300 nm)/Si substrate does contain some carbon around 1 EGM. After the Ni deposition on SiO₂(300 nm)/Si substrate, around 3 EGM more are measured inside the Ni film. The carbon concentration after carbon implantation at room temperature increases by 4.6 EGM, instead of 4 EGM as expected. Thus, there is only a weak incorporation of carbon impurity during implantation at room temperature. After the implantation at 450 °C, a higher carbon incorporation rate (7 EGM instead of 4 EGM) is measured, suggesting carbon contamination due to the heating during the implantation. For higher implantation temperatures, the extra carbon incorporation rate $\Delta(C_i - C_{i-1})$ tends to decrease but still occurs, within the measurement uncertainty. Besides, after implantation at room temperature and subsequent annealing at 600 °C, the NRA analysis reveals a noticeable carbon contamination (10 EGM instead of 4 EGM). Comparing sample I-600 and I-RT-600 yields a net positive difference in carbon concentration of 2 EGM for the later sample. It is therefore more desirable to reduce the steps in order to limit that additional carbon incorporation. In conclusion,

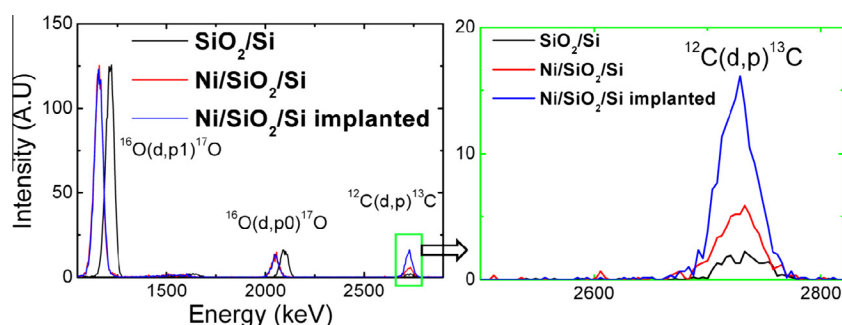


Fig. 2 – NRA spectra obtained with a deuteron beam at 900 keV on the SiO₂(300 nm)/Si, Ni(200 nm)/SiO₂(300 nm)/Si and I-RT samples. The ¹²C(d, p)¹³C reaction is zoomed on the right figure.

Table 1 – Carbon concentrations obtained from experimental NRA spectra analyzed by SAM software. The corresponding EGM measured by NRA, and the expected one without additional carbon incorporation with the exception of carbon implantation, are reported. $\Delta(C_i - C_{i-1})$ corresponds to the EGM increase after each step i of a sequence of preparation defined in Fig. 1.

Sample	C conc. measured (10^{15} at.cm $^{-2}$)	EGM measured	EGM expected	$\Delta(C_i - C_{i-1})$ measured	$\Delta(C_i - C_{i-1})$ expected
SiO $_2$ (300 nm)/Si	4	1	0	1	0
Ni(200 nm)/ SiO $_2$ (300 nm)/Si	15	4	0	3	0
I-RT	31	8.6	4	4.6	4
I-450	40	11	4	7	4
I-525	33	9	4	5	4
I-600	30	8	4	4	4
I-RT-600	37	10	4	1.4	0
EGM	3.6	1	–	–	–

carbon extra-incorporation occurs at each step of the process: during the Ni evaporation, the carbon implantation in temperature and the post-annealing treatment. Finally, more than twice the expected carbon concentration is measured at the end of the process in average. Therefore, there is a need to improve the purity of the sample at each step of the process.

Fig. 3 shows SEM micrographs at different magnitudes of the I-450 (a and b), I-525 (c and d) and I-600 (e–g) samples obtained by using the Secondary Electron Detector at 3 kV.

We remark high surface contrasts and a morphology evolution with the implantation temperature. The dark fragments in Fig. 3a, c and e could be assigned to graphitic-like carbon fragments or multi-layer graphene. On the I-450 sample, these dark fragments are located mainly at grain bound-

aries as they are induced by carbon diffusion to the surface through the grain boundaries. This preferential location is no more observed for higher temperatures. On the I-525 sample, the dark fragments expand now above the nickel grains (Fig. 3c and d). It is also noticed that these fragments are rather shapeless, as their edges are not very well structured. Inside these shapeless fragments, high contrast could sometimes be observed, as pointed by white arrows in Fig. 3d. These contrasts could be related to changes in the thickness of the graphene layers, as reported in the literature by SEM [33]. The estimated sizes range from 500 nm to several micrometers. On the I-600 sample the increase of temperature induces a progressive structuration of these graphitic fragments (Fig. 3e and g). Most of the fragments display now faceted edges with angles equal or multiples of 60°, as

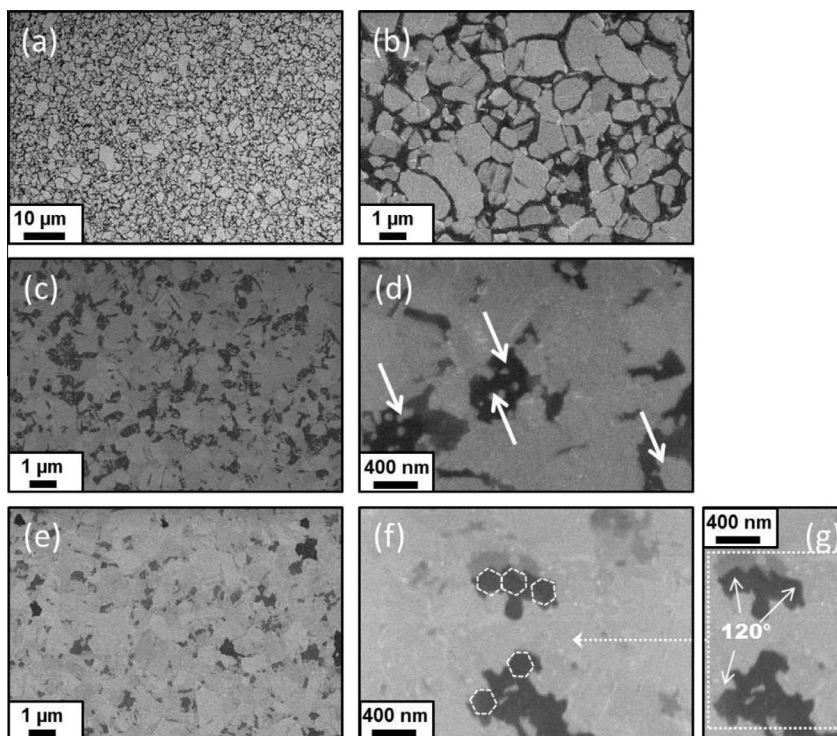


Fig. 3 – SEM micrographs at 3 kV of I-450 (a and b), I-525 (c and d) and I-600 (e–g) samples at different magnitudes. Arrows on (d) underline bright contrast inside a dark fragment. In (f) the MLG fragments of (g) are delimited with white dashed lines to underline the facets with 120° angles.

expected from the hexagonal structure of graphite (Fig. 3g and f with white underlining). Brighter areas are no longer observed inside the fragments but rather now on the periphery of the fragments. Similar shape variations have been reported for the CVD graphene grown on copper in the literature [34].

From AFM measurements (some images are displayed in Supplementary Materials S2), the mean roughness on $10 \times 10 \mu\text{m}^2$ area, after carbon implantation, are quoted to 6.3 ± 1.5 , 30.6 ± 1.9 , 11.3 ± 2.3 and 6.7 ± 1.4 nm for the I-RT, I-450, I-525 and I-600 samples, respectively. By contrast the mean roughness are quoted to 3.7 ± 2.1 nm on $\text{SiO}_2(300 \text{ nm})/\text{Si}$ and 3.6 ± 1.2 nm on bare $\text{Ni}(200 \text{ nm})/\text{SiO}_2(300 \text{ nm})/\text{Si}$ samples. Comparing bare sample and implanted samples shows that carbon implantation induces a higher roughness. This is probably due to some sputtering. A progressive decrease of the roughness occurs with increasing implantation temperature.

In order to determine if the surface evolution is directly correlated to some carbon structuration, Raman analysis was carried out. Fig. 4 displays for the three samples (I-450, I-525 and I-600) the Raman mapping of the 2D band within the $2695\text{--}2725 \text{ cm}^{-1}$ range (Fig. 4b, f, j); the Raman mapping of the G band within the $1560\text{--}1590 \text{ cm}^{-1}$ range (Fig. 4c, g, k) together with the corresponding optical images (Fig. 4a, e, i). The maps are recorded over an area of $100 \mu\text{m}^2$ with increasing intensities ranging from dark to bright blue. Moreover, to illustrate the contrast between the darker and lighter areas

observed on the optical images, several characteristic Raman spectra are reported in Fig. 4d, h, l.

The G band is a one-mode Raman vibration characteristic of graphitic carbon [35]. The 2D band is a multiple step mode of carbon vibration whose intensity, shape and wave number are sensitive to the interaction with the substrate, to the thickness of the graphene layers and to the presence of either impurities, doping atoms, vacancies or functionalized molecules [32,36–39]. Finally as soon as graphite displays either structural defects or size-limited dimensions, a D band appears around 1350 cm^{-1} [40].

On the I-450 sample, the Raman mapping highlights a heterogeneous surface with a difference across a Ni grain from the center (bright) to the boundary (dark) of the grain. The reverse contrast is generally observed in the G and 2D bands maps. Raman spectra recorded on the grain boundaries exhibit two wide D and G contributions at $\sim 1370 \text{ cm}^{-1}$ and at $\sim 1570 \text{ cm}^{-1}$, respectively, and a small 2D one at $\sim 2700 \text{ cm}^{-1}$. The I_D/I_G ratio is evaluated to be 1.4 and the FWHM of both the D and G bands are around 230 and 100 cm^{-1} , respectively (Table 2 and Fig. 4d).

By contrast, Raman peaks cannot be observed inside the nickel grain. These results indicate the presence of amorphous carbon or small badly-structured graphitic domains at grain boundaries, which is in good agreement with the SEM observations (Fig. 3b).

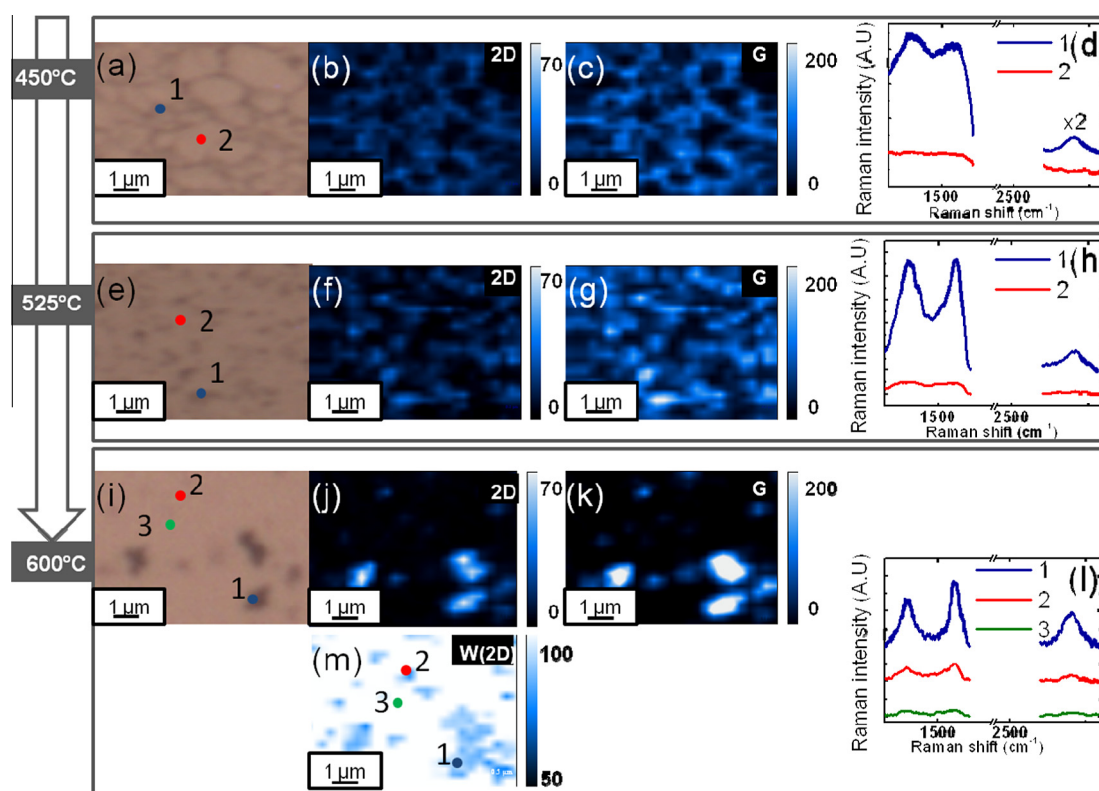


Fig. 4 – (a, e, i) Optical images; (b, f, j) corresponding Raman mapping on the 2D band; (c, g, k) corresponding Raman mapping on the G band and (d, h, l) Raman spectra on different labeled dots of the surface (blue: dark zone; red: bright or slightly contrasted zone; green: bright zone) on images a, e and i, respectively. Bottom: Raman mapping on the Full Width at Half-Maximum (FWHM) of the 2D band of the I-600 sample (m). (a–d): I-450; (e–h): I-525 and (i–m): I-600 samples, respectively. A colour version of this figure can be viewed online.

Table 2 – Raman features (ratio of intensities I_D/I_G and I_{2D}/I_G ; FWHM (W) of the D, G, and 2D bands for the I-450, I-525, I-600 and I-RT-600 samples, respectively. For the I-600 and I-RT-600 samples, the dots1 and 2 correspond to dark and bright fragments, respectively.

Samples	I_D/I_G	I_{2D}/I_G	W_D (cm ⁻¹)	W_G (cm ⁻¹)	W_{2D} (cm ⁻¹)
I-450 (Dot1)	1.4	0.02	230	100	–
I-525 (Dot1)	0.9	0.05	160	90	–
I-600 (Dot1)	0.6	0.4	60	50	51
I-600 (Dot2)	0.9	0.8	120	80	60
I-RT-600 (Dot1)	0.8	0.5	110	50	100
I-RT-600 (Dot2)	0.3	0.6	50	30	60

The implantation at 525 °C leads to the formation of small dark fragments with a large density (Fig. 4e–h). On these dark fragments, besides thinner D and G features, the small contribution attributed to 2D band appears more clearly at ~ 2700 cm⁻¹. The ratio I_D/I_G obtained for the dark fragments in the optical image decreases from 1.4 to 0.9. These results underline the presence of better-structured graphite fragments.

The Raman spectra of the sample I-600 recorded on the darker fragments displays now distinct D, G and 2D contributions (Fig. 4l). However the relative intensity of the D contribution decreases. Indeed, the ratio I_D/I_G decreases down to 0.6 (Table 2). This drop of the D band indicates most likely a pronounced graphitization of the fragments soon observed at 525 °C. W_G decreases to around 60 cm⁻¹ and often a small shoulder can be observed around 1615 cm⁻¹, maybe due to some wrinkling or folding of the graphitic fragments. This band, defined as D' in the literature, could be explained by some curvature of the graphitic fragments [37]. Moreover, the 2D band intensity clearly increases and the ratio I_{2D}/I_G increases, but still remains around 0.4. Comparison between Fig. 4f–h and Fig. 4j–l reveals that the graphitic fragments are thinner and better organized at 600 °C. The symmetry of the 2D band as well as the low ratio I_{2D}/I_G both indicates that the graphitic fragments are turbostratic as they display no ordering between the stacked graphene plans [36,37]. The Raman spectrum corresponding to a bright zone in the optical image (zone 2) exhibits D, G and 2D contributions (Fig. 4l) with quite different characteristics compared to those determined on the dark fragment (zone 1). Indeed, in this last case the intensities are larger, the ratios I_D/I_G and I_{2D}/I_G decrease and W_D as well as W_{2D} are narrower.

To illustrate the 2D band evolution, Fig. 4m shows a color map of W_{2D} ranging from 100 cm⁻¹ (white) to 50 cm⁻¹ (blue), corresponding to weak and better ordered MLG layers, respectively. The data show that the low W_{2D} domains (blue spots) are expanded around the fragment identified in the optical image (Fig. 4i). We can conclude that the graphitic fragments observed on the optical image are surrounded by thinner graphite layers that are hardly revealed by optical microscopy. This result is well correlated by the SEM observations (Fig. 3f) and tends to confirm some structuring with thinner and better ordered graphene layers on the edges of the fragment.

Thus it appears that the carbon diffusion towards surface induces the formation of graphitic fragments observed as soon as 450 °C. For higher implantation temperatures, a struc-

turing of these fragments occurs due most likely to fragment coalescence and leading to turbostratic graphitic domains.

To investigate further the synergetic effect of temperature and implantation, one sample was implanted at RT and subsequently in situ heated at 600 °C. Fig. 5 displays the SEM images obtained for this I-RT-600 sample.

The SEM micrographs reveal clear differences between the I-RT-600 sample (Fig. 5a and b) and the I-600 sample displayed in Fig. 3e and f, and Fig. 5c. The dark fragments observed on both samples display different shapes and different densities. Unlike the I-600 sample, the fragments present rather identical contrasts. Therefore, the fragments counting and size distribution could be determined using ImageJ software (Fig. 5d). Two size populations are reported: very small fragments with mean area around 0.015 ± 0.012 μm^2 and larger fragments with mean areas around 0.12 ± 0.03 μm^2 , corresponding to mean sizes of 140 and 390 nm, respectively. It is not possible to estimate the size distribution for the I-600 sample because the contrast with the substrate is poor and the edges are not so well defined. However, the fragments for the I-RT-600 sample are smaller but the density is larger than for the I-600 sample. We also remark that most of the fragments have an oval shape with multiple of 60° as edges and even few of them display hexagonal shapes (Fig. 5b). As it was observed before, the Raman spectra performed on dark fragments show D, G and 2D bands (Fig. 5e). On Fig. 5e, the spectrum 1 is recorded on a small dark fragment with an oval shape. The spectrum 2 is acquired on a brighter MLG fragment presenting faceted edges. A clear difference is observed as for the faceted fragment the D band decreases strongly and the G band is narrowed (Table 2). If we compare the Raman spectra of the I-RT-600 sample with those of the I-600 sample, it can be noted that the W_{2D} are slightly wider (60–80 cm⁻¹) than on the I-600 (50–60 cm⁻¹). In conclusion the two kinds of fragments observed by SEM and Raman analyses are correlated with two mechanisms of carbon diffusion and graphene nucleation. The smaller ones, less structured and more abundant, could be attributed to carbon segregation on the surface coming mainly from adventitious carbon. By contrast, the largest faceted ones could be formed by the diffusion of the implanted carbon towards the surface.

Finally we have estimated the mean thickness e of surface carbon by angular X-ray Photoelectron Spectroscopy (XPS) measurements on the I-600 sample (Fig. 6). The XPS carbon signal C1s obtained on this signal I_{Gene} is continuously recorded with the C1s signal of HOPG reference graphite I_{Gite} .

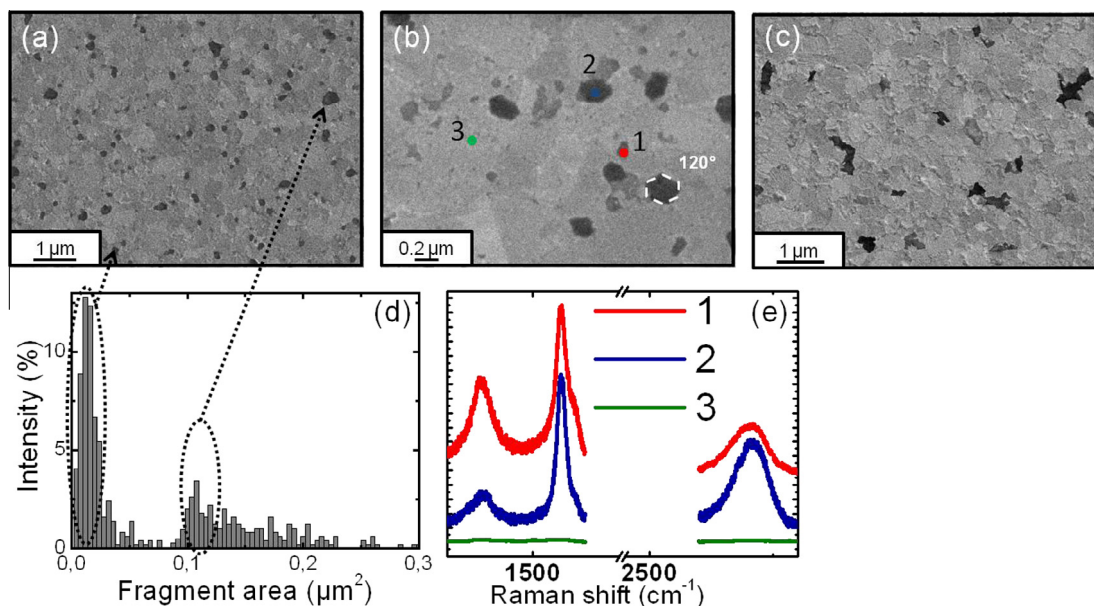


Fig. 5 – SEM micrographs of MLG fragment for the (a and b) I-RT-600; (c) I-600 samples; (d) fragments area distribution and (e) Raman spectra of I-RT-600 sample on dots displayed in (b). The white hexagon on (b) underlines faceted edge angles of around 120°. Note that the surface distribution of the MLG fragments in (d) (491 fragments) is bimodal.

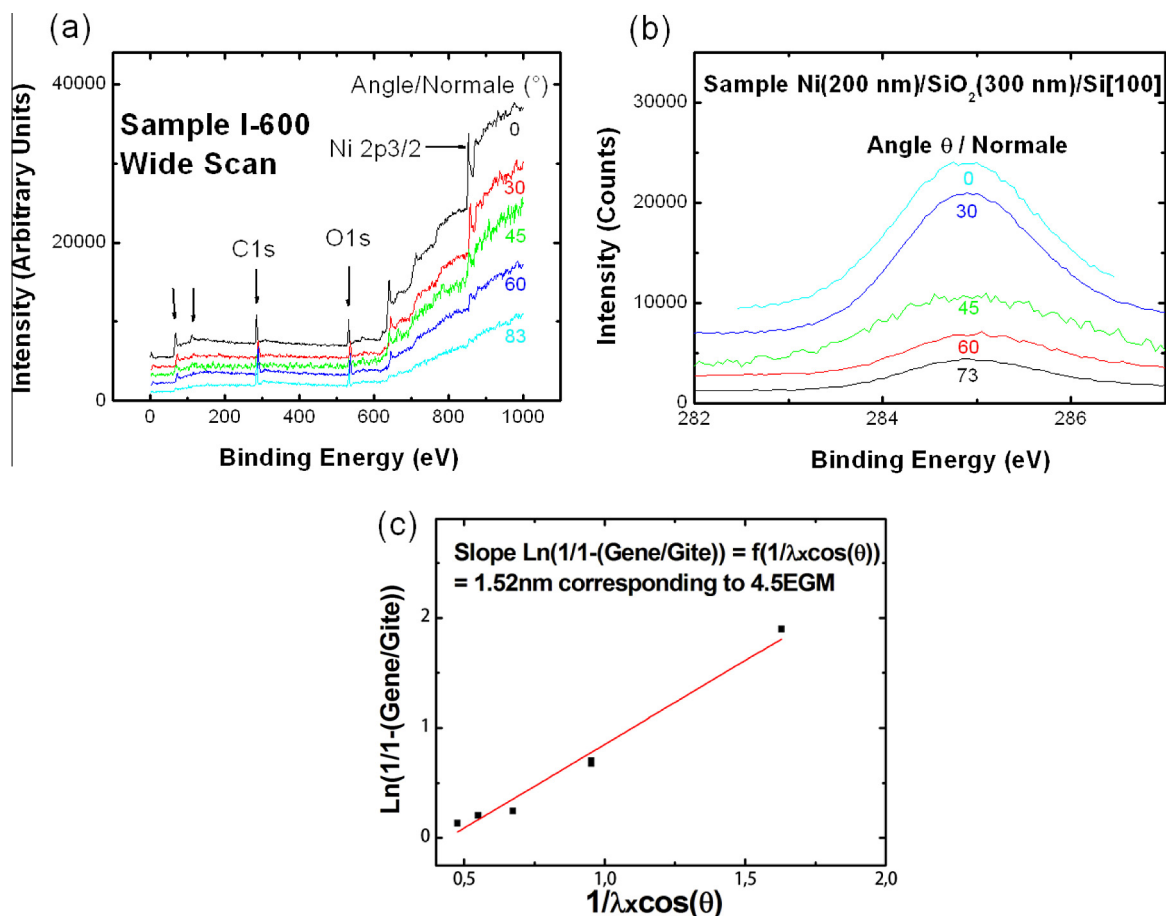


Fig. 6 – XPS spectra on I-600 sample as a function of the angle θ of the detector with the normal of the surface. Sequence of (a) Wide scans; (b) C1s spectra and (c) Plot of $\ln(1/1 - (I_{\text{Gene}}/I_{\text{Gite}})) = f(1/\lambda_c \cos \theta)$ whose slope yields a mean surface carbon thickness (4.5 EGM).

Assuming that the mean free path of the inelastic process of carbon λ_C is the same on both samples, the thickness e can be extracted from the ratio $I_{\text{Gene}}/I_{\text{Gite}}$ by the following relation (see [Supplementary Materials S3](#))

$$\ln(1/(1 - (I_{\text{Gene}}/I_{\text{Gite}}))) = e/\lambda_C \cdot \cos \theta \quad (1)$$

where θ is the angle of the detector with the normal to the surface of the sample. The mean thickness is thus extracted from the slope of the plot of Eq. (1) ([Fig. 6c](#)) with $\lambda_C = 2.1 \text{ nm}$ [41]. The mean thickness extracted is quoted to 4.5 EGM. This value is in rather good agreement with the dose of implanted carbon (around 4 EGM), but lower than the measured amount of carbon by NRA estimated to 8 EGM. However, we must remind that NRA encompass both surface and bulk carbon. Therefore, it is presumed that some carbon remains diluted into the Ni matrix.

4. Discussion

The literature has soon described the formation of MLG layers by carbon implantation into carbon-diffusive metallic matrices like Ni [25–28]. In all these references, a nickel film of variable thickness, from 50 to 500 nm, is deposited on a $\text{SiO}_2(300 \text{ nm})/\text{Si}(100)$ substrate. A thermal annealing at 1000 °C under H_2/Ar is preliminary achieved in order to grow the Ni grains deposited at room temperature in [25,27]. Implantations were achieved at room temperature with carbon dose within 0.003–4 EGM at variable energies in the range 5–120 keV. Finally in all cases, a post-thermal treatment is subsequently performed at temperatures above or equal to 600 °C, either under vacuum or with a H_2/Ar environment. During these post-thermal treatments, the morphology of the nickel film, the temperature and the cooling rate are critical parameters. MLG fragments are obtained with good quality above 600 °C but are formed heterogeneously on the surface. This heterogeneity can be explained by the occurrence of different nucleation sites for carbon and a preferential carbon migration along the grain boundaries [16,42]. The same is also observed in our case even after implantation at high temperature. Clearly an improvement of the morphology of the metallic layer is required to avoid the formation of grain boundaries. In our specific case however, the step of post-thermal treatment is avoided by direct implantation at high temperatures. Therefore, we are free from the temperature-dependent processes of carbon bulk diffusion and surface segregation [43]. The maximum temperature of 600 °C was chosen as at this temperature one monolayer graphene is expected to be stable at the nickel surface. Above around 700 °C, the graphene layer would be no longer stable, as reported by XPS in temperature. Above around 823 °C the graphene layer on a Ni(111) surface is not yet stable [44].

However, as evidenced by the Raman mapping, the thickness and even the quality of the MLG fragments are variable. A progressive structuration is observed with increasing the implantation temperature, as ascertained by the appearance of well-defined edges in the MLG fragments at 600 °C and a progressive narrowing of the G and 2D bands. Two reasons can explain this behavior: (1) First, the grain boundaries on

nickel are preferential sites for graphite nucleation. Thus the MLG fragments are first formed on the grain boundaries (450 °C), then they diffuse along the grain (525 °C) and finally rather homogeneous domains are obtained at 600 °C. (2) Second, the total amount of carbon largely exceeds the expected amount of carbon. Indeed, the carbon concentration at the surface and inside the metallic Ni matrix, determined by NRA, is varying but still remains at a large level. This could explain also the bimodal fragment distribution on I-RT-600 sample as the small fragments can be correlated with the high content of carbon impurity. There is clearly a need to control the incorporation of carbon at each step of the process. Does it mean however that graphene growth would be possible without carbon implantation? The answer is not so simple. Carbon atoms as impurities are randomly trapped in bulk Ni, as shown by channeling NRA experiments. However the formation of MLG fragments has never been observed without implantation [45]. Carbon from impurities may diffuse and segregate to the surface, but cannot aggregate as graphene precursor due to low carbon density. Reversely, surface segregation from graphene precursor is possible after carbon implantation due to the high localized concentration of carbon into nickel that diffuses to the surface.

Obviously, the carbon impurity incorporation can affect other processes of graphene or MLG formation. It was thus reported that graphene can be obtained by diffusion through either copper or nickel films from a solid source on the opposite side [21–23]. When graphene is formed by simple diffusion from a carbon source through nickel at room temperature, it is not clear however if the carbon is coming either from carbon impurity inside the nickel or from the carbon solid source [23].

Moreover, we can independently compare the total amount of carbon present both at the surface and inside the metallic Ni matrix, determined by NRA, with the carbon surface concentration alone determined by angular XPS from the thickness of the MLG film. Indeed, the overall carbon concentration is quoted to 7 EGM, while the carbon surface concentration is determined to 4–5 EGM. From these independent results, it is possible (See [Supplementary Materials S4](#)) to evaluate the bulk carbon concentration inside the Ni film. This bulk atomic ratio C/Ni is then estimated to be around $(0.8 \pm 0.2)\%$, in rather good agreement with the presence of a solid solution of carbon inside the nickel film [46,47]. We must remind however that this analysis is a rough overestimation, as XPS is sensitive to carbon up to around 5 nm and some carbon may also migrate at the interface between the nickel film and the substrate.

5. Conclusion

The main conclusions and future perspectives of this paper are as follows:

- Carbon implantation on Ni(200 nm)/ $\text{SiO}_2(300 \text{ nm})/\text{Si}$ substrates at different temperatures (450–600 °C) with a carbon dose of 4 EGM gives MLG fragments by diffusion to the surface.

- The heterogeneity of these MLG is due to preferential carbon diffusion through grain boundaries. To avoid it, monocrystalline Ni(111) or Cu(111) films grown on monocrystalline substrates like MgO(111) or Al₂O₃(111) [35] are under investigation [45].
- A progressive structuration of these fragments with increasing the implantation temperature occurs.
- The mean carbon surface concentration is determined to around 4–5 EGM by angular X-ray Photoemission Spectroscopy (XPS).
- The overall carbon concentration, both inside and at the surface of the Ni films, was quoted by nuclear reaction analysis (NRA) from 7 to 10 EGM, depending on the temperature, but always exceeding the expected carbon concentration.
- This discrepancy shows that some carbon is incorporated along the different steps of the process and is involved into the MLG formation. These results points to the necessity to control the carbon incorporation at any step of the process and to know the full system C–Ni in the preparation of graphene or MLG to obtain uniform films.
- Further improvement in the control of carbon impurity incorporation is in progress, especially by the use of labeled experiments with ¹³C [48] to detect the contributions coming either from spurious or implanted carbon. Moreover the use of Ultra High Vacuum set up with a high level of pressure control would prevent undesired carbon incorporation.

Acknowledgements

J. Faerber (IPCMS, Strasbourg), S. Zafeiratos (ICPEES, Strasbourg) and P. Kern (ICube) are acknowledged for their help in SEM, XPS and AFM investigations, respectively.

Appendix A. Supplementary data

Supplementary data associated with this article can be found, in the online version, at <http://dx.doi.org/10.1016/j.carbon.2013.07.106>.

REFERENCES

- [1] Novoselov KS, Geim AK, Morozov SV, Jiang D, Zhang Y, Dubonos SV, et al. Electric field effect in atomically thin carbon films. *Science* 2004;306(5696):666–9.
- [2] Avouris P, Dimitrakopoulos C. Graphene: synthesis and applications – review article. *Mat Today* 2012;15(3):86–97.
- [3] Hernandez Y, Nicolosi V, Lotya MA, Blighe FM, Sun ZY, De S, et al. High-yield production of graphene by liquid-phase exfoliation of graphite. *Nat Nanotechnol* 2008;3:563–8.
- [4] Lotya MA, Hernandez Y, King PJ, Smith RJ, Nicolosi V, Karlsson LS, et al. Liquid phase production of graphene by exfoliation of graphite in surfactant/water solutions. *J Am Chem Soc* 2009;131(10):3611–20.
- [5] Choi WB, Lahiri W, Seelaboyina R, Kang YS. Synthesis of graphene and its applications: a review. *Crit Rev Solid State Mater Sci* 2012;35(1):52–71.
- [6] Wang X, Zhi LJ, Mullen K. Transparent. Conductive graphene electrodes for dye-sensitized solar cells. *Nano Lett* 2008;8(1):323–7.
- [7] Berger C, Song Z, Li TB, Li XB, Ogbazghi AY, Feng R, et al. Ultrathin epitaxial graphite: 2D electron gas properties and a route toward graphene-based nanoelectronics. *J Phys Chem B* 2004;108(52):19912–6.
- [8] First PN, Strosio JA, De Heer WA, Seyller T, Berger C, Moon JS. Epitaxial graphene on silicon carbide. *MRS Bull* 2010;35(4):296–305.
- [9] Emtsev KV, Bostwick A, Horn K, Jobst J, Kellogg JL, Ley L, et al. Towards wafer-size graphene layers by atmospheric pressure graphitization of silicon carbide. *Nat Mat* 2009;8:203–7.
- [10] Obratsov AN, Obratsova ED, Zolotukhin AA, Tyurnina AV. Chemical vapor deposition of thin graphite films of nanometer thickness. *Carbon* 2007;45(10):2017–21.
- [11] Yu Q, Lian J, Siriponglert S, Li H, Chen YP, Pei SS. Graphene segregated on Ni surfaces and transferred to insulators. *Appl Phys Lett* 2008;93(11):113103–6.
- [12] Reina A, Jia X, Ho J, Nezich D, Son H, Bulovic V, et al. Large area, few-layer graphene films on arbitrary substrates by chemical vapor deposition. *Nano Lett* 2009;9(1):30–5.
- [13] Kim KS, Zhao Y, Ahn JH, Jang H, Lee SY, Kim JM, et al. Large-scale pattern growth of graphene films for stretchable transparent electrodes. *Nature* 2009;457:706–10.
- [14] Chae SJ, Gunes F, Kim KK, Kim ES, Han GH, Kim SM, et al. Synthesis of large-area graphene layers on poly-nickel substrate by chemical vapor deposition: wrinkle formation. *Adv Mater* 2009;21(22):2328–33.
- [15] Zhang Y, Gomez L, Ishikawa FN, Madaria A, Ryu KM, Wang C, et al. Comparison of graphene growth on single-crystalline and polycrystalline Ni by chemical vapor deposition. *J Phys Chem Lett* 2010;1:3101–7.
- [16] Baraton L, Maurice JL, Lee CS, Cojocaru CS, Chatelet M, Pribat D, et al. On the mechanisms of precipitation of graphene on nickel thin films. *Eur Phys Lett* 2011;96(4):46003.
- [17] Lee CS, Cojocaru CS, Moujahid W, Lebental B, Chaigneau M, Chatelet M, et al. Synthesis of conducting transparent few-layer graphene directly on glass at 450 °C. *Nanotechnology* 2012;23(26):265603–9.
- [18] Lee YB, Bae SK, Jang H, Jang SJ, Zhu SE, Sim SH, et al. Wafer-scale synthesis and transfer of graphene films. *Nano Lett* 2010;10(2):490–3.
- [19] Mattevi C, Kim HK, Chhowalla M. A review of chemical vapour deposition of graphene on copper. *J Mater Chem* 2011;21:3324–34.
- [20] Hofrichter J, Otto M, Szafrank BN, Echtermeyer TJ, Baus M, Majerus A, et al. Synthesis of graphene on silicon dioxide by a solid carbon source. *Nano Lett* 2010;10(1):36–42.
- [21] Sun Z, Zheng Y, Yao J, Beitler E, Zhu Y, Tour JM. Growth of graphene from solid carbon sources. *Nature* 2010;468:549–52.
- [22] Ruan GD, Sun ZZ, Peng ZW, Tour JM. Growth of graphene from food, insects, and waste. *ACS Nano* 2011;5:7601–7.
- [23] Kwak J, Chu JH, Choi JK, Park SD, Go HS, Kim SY, et al. Near room-temperature synthesis of transfer-free graphene films. *Nat Commun* 2012;3:645.
- [24] Baraton L. Process for controlled growth of graphene films. International Patent 0805769, 2008.
- [25] Garaj S, Hubbard W, Golovchenko JA. Graphene synthesis by ion implantation. *Appl Phys Lett* 2010;97(18):183103–6.
- [26] Baraton L, He Z, Lee CS, Maurice JL, Cojocaru CS, Gourgues-Lorenzon AF, et al. Synthesis of few-layered graphene by ion implantation of carbon in nickel thin films. *Nanotechnology* 2011;22(8):085601–85606.
- [27] Mun JH, Lim SK, Cho BJ. Local growth of graphene by ion implantation of carbon in a nickel thin film followed by rapid thermal annealing. *J Electrochem Soc* 2012;159(6):G89–92.

- [28] Zhang R, Zhang ZD, Wang ZS, Wang SX, Wang W, Fu DJ, et al. Non linear damage effect in graphene synthesis by C-cluster ion implantation. *Appl Phys Lett* 2012;101(1):011905.
- [29] Aweke F, Gutierrez G, Lee CS, Cojocaru CS, Le Normand F, Muller D, Speisser, et al. to be published.
- [30] Ziegler JF, Biersack JP, Littmark U. *Rutherford backscattering spectrometry*. New York, Annexe: Pergamon Press; 1985.
- [31] Stoquert JP, Pecheux F, Herve Y, Marchal H, Stuck R, Siffert P. VRBS: a virtual RBS simulation tool for ion beam analysis. *Nucl Instrum Meth B* 1998;1152:136–8.
- [32] Ferrari AC, Novoselov KS, Geim AK, Meyer JC, Roth S, Scardaci V, et al. Raman spectrum of graphene and graphene layers. *Phys Rev Lett* 2006;97:187401–4.
- [33] Park MH, Kim TH, Yang CW. Thickness contrast of few-layered graphene in SEM. *Surf Interface Anal* 2012;44:1538–41.
- [34] Ago H, Ogawa Y, Tsuji M, Mizuno S, Hibino H. Catalytic growth of graphene: toward large-area single-crystalline graphene. *J Phys Chem Lett* 2012;3:2228–36.
- [35] Tuinstra F, Koenig JL. Raman spectrum of graphite. *J Chem Phys* 1970;53(3):1126–31.
- [36] Malard LM, Pimenta MA, Dresselhaus G, Dresselhaus MS. Raman spectroscopy in graphene. *Phys Rep* 2009;473:51–87.
- [37] Pimenta MA, Dresselhaus G, Dresselhaus MS, Cancado LG, Jorio A, Saito R. Studying disorder in graphite-based systems by Raman spectroscopy. *Phys Chem Chem Phys* 2007;9(11):1276–91.
- [38] Cancado LG, Jorio A, Ferreira EH, Stavale F, Achete CA, Capaz RB, et al. Quantifying defects in graphene via Raman spectroscopy at different excitation energies. *Nano Lett* 2011;11:3190–6.
- [39] Calizo I, Bao W, Miao F, Lau CN, Balandin AA. The effect of substrates on the raman spectrum of graphene: graphene-on-sapphire and graphene-on-glass. *Appl Phys Lett* 2007;91:201904.
- [40] Ferrari AC, Robertson J. Resonant Raman spectroscopy of disordered, amorphous, and diamond like carbon. *Phys Rev B* 2001;64:075414–75426.
- [41] Tanuma S, Powell CJ, Penn DR. Calculations of electron inelastic mean free paths. V data for 14 organic compounds over the 50–2000 eV range. *Surf Interface Anal* 2004;21:165–76.
- [42] Han GH, Gunes F, Bae JJ, Kim ES, Chae SJ, Shin HJ, et al. Influence of copper morphology in forming nucleation seeds for graphene growth. *Nano Lett* 2011;11:4144–8.
- [43] Usachov D, Vilkov O, Gruneis A, Haberer D, Fedorov A, et al. Nitrogen-doped graphene: efficient growth, structure, and electronic properties. *Nano Lett* 2011;11(12):5401–7.
- [44] Fujita D, Yoshihara K. Surface precipitation process of epitaxially grown graphite (0001) layers on carbon-doped nickel (111) surface. *J Vac Sci Technol* 1994;12(4):2134–40.
- [45] Speisser C, Arabski J, Morvan G, Aweke F, Benyahia M, Le Normand F. to be published.
- [46] Eizenberg M, Blakely JM. Carbon monolayer phase condensation on Ni(111). *Surf Sci* 1979;82(1):228–36.
- [47] Hansen M, Anderko K. *Constitution of binary alloys. Ni-C system* 2nd ed Metallurgy and metallurgical engineering. 2nd Ed. New York: Mac Graw-Hill; 1959:374.
- [48] Gutierrez G, Aweke F, Muller D, Antoni F., Le Normand F. submitted.